

Nematic Order in Small Systems: Measuring the Elastic and Wall-Anchoring Constants in Vibrofluidized Granular Rods

Jennifer Galanis,¹ Ralph Nossal,² Wolfgang Losert,³ and Daniel Harries¹

¹*Institute of Chemistry and The Fritz Haber Center, The Hebrew University, Jerusalem, 91904, Israel*

²*Program in Physical Biology, National Institute of Child Health and Human Development, NIH, Bethesda, Maryland 20892-0924, USA*

³*Department of Physics, IPST, and IREAP, University of Maryland, College Park, Maryland 20742, USA*
(Received 16 March 2010; revised manuscript received 22 August 2010; published 13 October 2010)

We investigate nematic order in vibrated granular rods confined to a small quasi-2D container less than 10 rod lengths in diameter. As rod density ρ increases, patterning shifts from bipolar to uniform alignment. We find that a continuum liquid crystal free energy functional captures key patterning features down to almost the particle size. By fitting theory to experiments, we estimate the relative values of bend and splay elastic constants and wall anchoring. We find that splay is softer than bend for all ρ and rod lengths tested, while the ratio of the average elastic constant to wall anchoring increases with ρ .

DOI: 10.1103/PhysRevLett.105.168001

PACS numbers: 45.70.Qj, 05.65.+b, 61.30.-v

While mechanically driven granular materials display many phenomena that highlight their nonequilibrium nature [1], equilibriumlike behavior can be observed under certain experimental conditions [2]. The analogy between patterning in granular materials and molecular or colloidal particles in equilibrium often occurs for entropy driven transformations, where mechanical agitation samples particle configurations that result from minimization of steric interactions [3,4]. For example, granular rods can behave like liquid crystals (LCs), with an isotropic-nematic transition that exhibits the expected scaling with rod length to diameter ratio (L/D) and density [3]. Knowledge of the LC elastic constants can further develop this analogy. In molecular LCs, the relative values of these constants control both static and dynamic material properties, such as distortions in various geometries [5] or defect dynamics [6].

Previous methods for measuring elastic constants are insufficient when applied to materials that are confined to a small space and consist of relatively few rods, N [7]. In our experiments (quasi-2D container, diameter $<10L$), boundary induced distortions in the nematic phase are often on the order of L and considered large. We, however, show that by taking ensemble averages, rod patterning resembles the field distortions observed in “larger” systems, such as LC droplets, where molecule size is much smaller than droplet dimensions. The patterning in such droplets can be explained by minimizing a free energy functional, $\mathcal{F} = \mathcal{F}_{\text{bulk}} + \mathcal{F}_{\text{wall}}$, that considers both bulk and boundary rod alignment contributions [8–10].

For LCs, the Frank elastic free energy is commonly used to describe the energetic penalty for distortions in the bulk over an area A in two dimensions (2D) [11],

$$\mathcal{F}_{\text{bulk}} = \frac{1}{2} \int_A K_1 (\nabla \cdot \mathbf{n})^2 + K_3 (\nabla \times \mathbf{n})^2 dx dy, \quad (1)$$

where $\mathbf{n}(x, y) = [\cos\varphi, \sin\varphi]$ is the unit vector representing the local nematic director angle φ , and K_1 , K_3 are constants for splay and bend, respectively. The term for twist, which contains K_2 , is not present in 2D.

The form of $\mathcal{F}_{\text{wall}}$ is determined by boundary geometry and rod-boundary interactions [8–10]. For simple steric interactions that favor rod alignment parallel to a hard immovable wall in 2D, the boundary term over the perimeter P can be approximated by

$$\mathcal{F}_{\text{wall}} = \frac{1}{2} C \int_P \sin^2(\varphi_w - \varphi) ds, \quad (2)$$

where C is a positive constant with units of line tension and φ_w describes the vector locally tangent to the wall. By adjusting K_1 , K_2 , and C so that the solution that minimizes \mathcal{F} matches the patterning observed in experiments, the relative values of the elastic constants and wall-anchoring strength of a material can be obtained [8].

We now apply a similar approach to measure the elastic constants and wall anchoring for our small, nonequilibrium granular system, demonstrating that the equilibrium description provides a valuable framework. By taking ensemble averages, we obtain the first quantitative measurements of nematic elastic constants and wall anchoring in granular materials. We find that, for rod densities and L/D tested, bend is significantly stiffer than splay. In addition, the average elastic constant increases relative to wall anchoring as rod density increases. Together, these three constants determine rod patterning.

Similar to methods in [3,4], we placed N steel rods ($D = 0.08$ cm, $L/D = 40$ and 60) into a quasi-2D circular container of area A (radius 15 cm). We focused on rod densities ρ above the nematic critical point [3], where $\rho = L^2 N/A$ is the normalized density that controls the 2D LC phase transition. The container was shaken with a sinusoidal oscillation of 50 Hz and a peak acceleration of

4 times gravity. Steady state in the rod patterning occurred in ≈ 5 min, and the position and orientation of each rod were found by an image processing algorithm.

Snapshots of granular rod arrangements in experiments are shown in Fig. 1, where $L/D = 40$ and $\rho = 15$, (a), and 30, (b). These images highlight different rod patterns that can occur by changing experimental conditions. At low ρ , Fig. 1(a), rod alignment is approximately straight in the center of the container, or “bulk,” but curves to follow the hard walls of the boundary. Where rod alignment between bulk and boundary compete to produce rod orientations perpendicular to the wall, two diametrically opposed point defects occur. We call this configuration “bipolar.” In contrast, the rods in Fig. 1(b) possess nearly uniform alignment throughout the entire container, with significant rod-boundary misalignment.

We will show that, on average, rod patterning resembles the minimized equilibrium continuum functional $\mathcal{F} = \mathcal{F}_{\text{bulk}} + \mathcal{F}_{\text{wall}}$, where the balance between $\mathcal{F}_{\text{bulk}}$ [Eq. (1)] and $\mathcal{F}_{\text{wall}}$ [Eq. (2)] controls spatial variations in the nematic

director. Minimizing \mathcal{F} with respect to \mathbf{n} yields the following Euler-Lagrange equations for the bulk

$$0 = -\frac{\partial^2 \varphi}{\partial x^2} (1 - \epsilon \cos 2\varphi) - \frac{\partial^2 \varphi}{\partial y^2} (1 + \epsilon \cos 2\varphi) + \epsilon \sin 2\varphi \left[-\left(\frac{\partial \varphi}{\partial x}\right)^2 + \left(\frac{\partial \varphi}{\partial y}\right)^2 + 2\frac{\partial^2 \varphi}{\partial x \partial y} \right] + 2\epsilon \cos 2\varphi \frac{\partial \varphi}{\partial x} \frac{\partial \varphi}{\partial y}, \quad (3)$$

and boundary

$$0 = Kx \left[\frac{\partial \varphi}{\partial x} (1 - \epsilon \cos 2\varphi) - \frac{\partial \varphi}{\partial y} \epsilon \sin 2\varphi \right] + Ky \left[-\frac{\partial \varphi}{\partial x} \epsilon \sin 2\varphi + \frac{\partial \varphi}{\partial y} (1 + \epsilon \cos 2\varphi) \right] - \frac{C}{2} \sin 2(\varphi_w - \varphi), \quad (4)$$

where $\epsilon = (K_1 - K_3)/(K_1 + K_3)$ is the elastic constant anisotropy, and $K = (K_1 + K_3)/2$ is the average elastic constant. As will be discussed, Fig. 1(c) and 1(d) compare the local orientation \mathbf{n} around continuum defects for experiments in Figs. 1(a) and 1(b), respectively (black lines) with the best fits to Eqs. (3) and (4) (red or gray lines).

As the energetic penalty for deformations in the bulk increases in comparison to the boundary, rod alignment changes from the pattern seen in Fig. 1(c) to that of 1(d). The balance between $\mathcal{F}_{\text{bulk}}$ and $\mathcal{F}_{\text{wall}}$ is mediated through K_1 , K_3 , and C [3,8–10]. In addition, anisotropy between K_1 and K_3 modifies the curvature of the distortion lines in rod patterning [8,10,12]. Conversely, by measuring changes in the nematic director through space, the values of these constants can be estimated. Since defects are relatively easy to locate and naturally provide large spatial variations in the nematic director, we employ a technique that investigates patterning around point defects to estimate the values of the constants [12].

To accurately identify defects in granular experiments, we define a local orientational order parameter $S(x, y, p) = \langle \cos 2\vartheta_i \rangle_p$ for all rods located within a distance p from (x, y) , where ϑ_i is the angle of the i th rod with the nematic director [5]. This yields a quantity that averages over many rods in an image and is defined for all (x, y) . We varied p and found that a value of $p = L$ allowed easy visualization of defects without excessive noise in the value of $S(x, y, p)$. The shading in Figs. 1(a), 1(b), and 1(e) corresponds to $S(x, y, p = L)$, where light to dark indicates high to low ordering. This method highlights two point defects in Fig. 1(a) (dark) that are analogous to the equilibrium solution. For $L/D = 40$, $\rho = 30$ and $L/D = 60$, $\rho \geq 25$, where nearly uniform alignment occurs, “defects” were defined by extending a line, whose orientation matched the bulk nematic director, from the center of the container to the boundaries.

The continuum model provides a description for two diametrically opposed defects that are either located at the

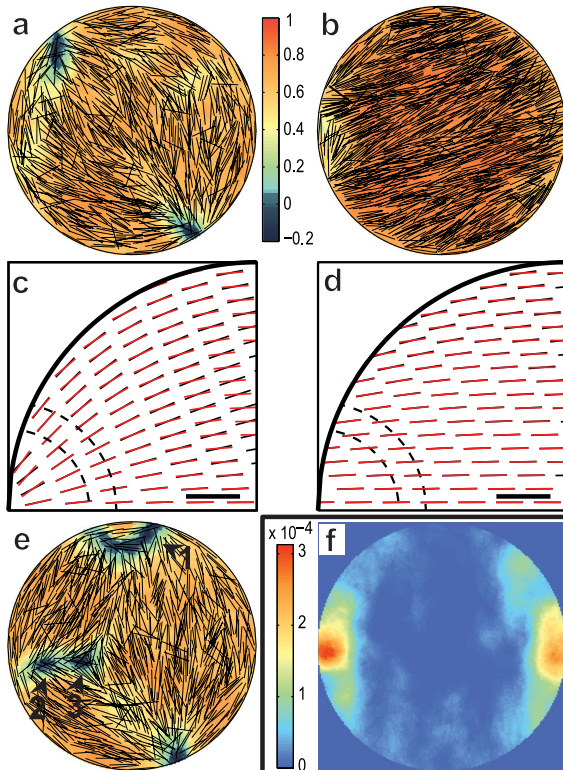


FIG. 1 (color online). Rod patterning in a circular container. For all images, $L/D = 40$. (a),(b) Snapshots of granular experiments for $\rho = 15$ and 30, respectively. Shading indicates local orientational order, $S(x, y, p = L)$. (c),(d) Local \mathbf{n} around continuum defects for experiments (black lines) and minimized free energy \mathcal{F} (red or gray lines) for $\rho = 15$ and 30, respectively (see text). Dashed arcs are at $1.5L$ and $2.0L$ from defect cores. Bars show rod length. (e) Snapshot depicts defects dissimilar to the continuum free energy minimum: line defect (arrow 1), a close pairing of two point defects (arrows 2,3), shown for $\rho = 15$. (f) Probability density of finding $S(x, y, p = L) < 0.2$ at a given location in the container for $\rho = 15$ (average of >500 images).

boundary, Fig. 1(c), or are virtual, “existing” outside the container, Fig. 1(d). In contrast, fluctuations in rod arrangements for the granular experiments can be significant, Fig. 1(e), and pattern matching with the continuum solution should only be expected for ensemble averages rather than for single instantaneous arrangements. By measuring the probability density of finding $S(x, y, p = L) < 0.2$, Fig. 1(f), we find that, on average, these granular experiments do contain only two diametrically opposed defects.

For the remainder of this manuscript, we focus on defects that resemble the continuum solution. We find “isolated” point defects, as seen in Figs. 1(a) and 1(e) (unlabeled defect) and define the center of each of these defects as the local minimum in $S(x, y, p = L)$. Figure 2(a) shows the probability of finding these defects a distance d from the container wall for $L/D = 40$ at various ρ . Because it is difficult to numerically evaluate Eq. (1) when the singularities associated with defect cores are located inside highly confined geometries [13], only defects located at the wall, $d < 0.25L$, were analyzed.

To characterize the nematic field near defects, we measured changes in the local director on arcs at distance r from each defect center, where θ is the positional angle and φ is the local nematic director orientation associated with

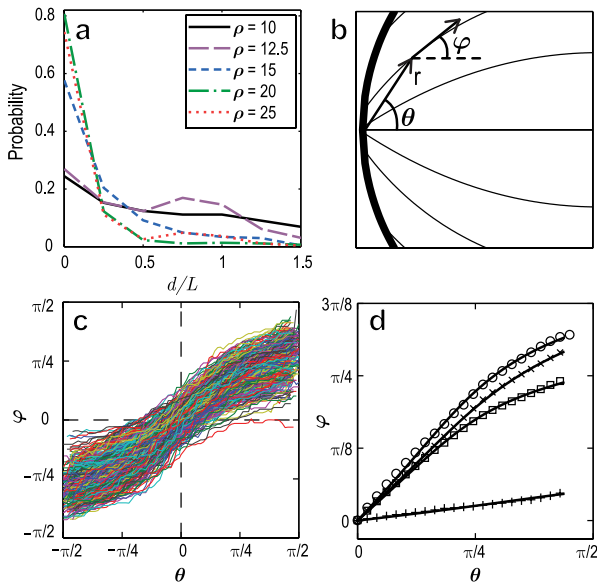


FIG. 2 (color online). Changes in nematic director orientation around point defects. For all plots, $L/D = 40$. (a) Probability distribution of finding equilibriumlike point defects in granular experiments as a function of the normalized d distance from the wall, d/L . (b) Schematic of a point defect at a boundary. We measure the orientation of the local nematic director, φ , on arcs located r distance from the center of the defect, where θ is with respect to the wall normal. (c) Variation of φ with θ at $r = 1.75L$ of all point defects at $\rho = 15$. (d) Variation of φ with θ at $r = 1.75L$ averaged over all point defects, for $\rho = 12.5$ (\circ), 15 (\times), 25 (\square), and 30 ($+$), with their corresponding fits to \mathcal{F} (lines). For each L/D and ρ , we collected >40 defects, with an average of ≈ 150 defects. Error bars, estimated using a bootstrapping method, fall within the symbol size.

$S(x, y, p)$, see Fig. 2(b). We set the direction normal to the wall as $\theta = 0$ and considered arcs within a band from $r = 1.5L$ to $2.0L$, Figs. 1(c) and 1(d). We excluded arcs $r < 1.5L$, since measurements on that scale most likely reflect individual rod stiffness rather than collective “nematic” behavior. Also, the fits are expected to be valid only in the vicinity of a defect, $r < 2.0L$, because we did not constrain for the presence of a second diametrically opposed defect in the experiments, while the numeric solution assumes both poles.

Figure 2(c) indicates φ versus θ at $r = 1.75L$ for all equilibriumlike defects collected at $\rho = 15$ for $L/D = 40$. This figure demonstrates large fluctuations in φ that can result from small N . Since we are interested in continuum-like behavior, we averaged these curves. Based on the symmetry of the solution, measurements from $\theta < 0$ were combined with those from $\theta > 0$. Figure 2(d) (symbols) shows the average change in φ with θ for $L/D = 40$ at several ρ . Material parameters can now be obtained from these curves.

Relative values of K_1 , K_3 , and C are determined as follows: Eqs. (3) and (4) are solved using a finite element method with two free parameters, ϵ and γ , where $\gamma = K/CA^{1/2}$ is the dimensionless ratio between the average elastic constant and wall anchoring. A modified Newton-Raphson method finds ϵ and γ that minimize the least square difference on all arcs, $r = 1.5L, 1.75L$, and $2L$, between the computed solution and experimental data (>190 data points per fit). As an example, the lines in Fig. 2(d) show results for $L/D = 40$ at $r = 1.75L$. The root mean squared error in φ for all the fits was <0.03 rad and <0.045 rad for $L/D = 40$ and 60 , respectively. The excellent agreement between experimental data and fits demonstrates that, on average, granular rod patterning is similar to the nematic continuum equilibrium solution.

Figures 3(a) and 3(b) show the extracted ϵ and γ , respectively, as a function of ρ . For $\rho < 30$, ϵ appears constant, Fig. 3(a) (open symbols), with an average value of -0.66 ± 0.04 (dotted line) and -0.76 ± 0.05 (dashed line) for $L/D = 40$ and 60 , respectively. These values signify that K_3 is appreciably stiffer than K_1 . For comparison, theory predicts ϵ for hard rods and prolate hard ellipsoids in 3D to be between -0.54 and -0.77 [14,15]. Also, simulations of prolate hard ellipsoids estimate ϵ between -0.14 to -0.59 [15], and experiments with tobacco mosaic virus measured ϵ to be ≈ -0.89 [16]. Excluded volume interactions dictate the values of K_1 and K_3 obtained in theory and simulations. These interactions also determine the degree of ordering S and depend on ρ and L/D [14,15]. However, the small variation in ϵ with ρ falls within our experimental uncertainty. For changes in L/D , simple mean field theories predict that while K_1 and K_3 both grow, ϵ remains constant [14]. Interestingly, our results suggest that when all interactions are considered, as realized in the experiment, ϵ too may vary with L/D , so that bend increases faster than splay.

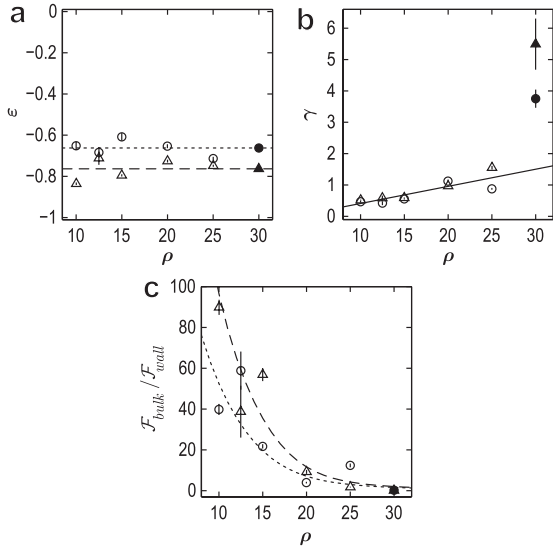


FIG. 3. Relative strength of elastic constants and wall anchoring in granular experiments. In all figures, open symbols [$L/D = 40$ (\circ), 60 (\triangle)] indicate a two parameter fit, ϵ and γ , of \mathcal{F} , while filled symbols show a single parameter fit, γ , for $\rho = 30$ where $\epsilon = -0.66$ (dotted line), -0.76 (dashed line) for $L/D = 40$ (\bullet), 60 (\blacktriangle), respectively (see text). (a) Elastic constant anisotropy ϵ as a function of ρ . (b) Dimensionless ratio of the average elastic constant to wall anchoring, γ , versus ρ . The line is a linear least squares fit of the data (all open symbols). (c) $\mathcal{F}_{\text{bulk}}/\mathcal{F}_{\text{wall}}$ versus ρ . Lines indicate the iso- ϵ curve for $\epsilon = -0.66$ (dotted), -0.76 (dashed), and the linear relation of γ versus ρ found in (b). Error bars in all graphs are determined by bootstrapping.

Figure 3(b) (symbols) shows an increase in γ with ρ . This means that K becomes stronger relative to C with increasing ρ . Therefore as ρ increases, the energetic penalties for deformations in the bulk nematic outweigh the energetic penalties for rod misalignment with the boundaries. This trend concomitantly causes a progressive decrease in $\mathcal{F}_{\text{bulk}}/\mathcal{F}_{\text{wall}}$ with ρ , Fig. 3(c) (open symbols). For $\rho < 30$, the trend in γ appears linear, where the line in Fig. 3(b) shows the least squares fit. Using this linear trend, we derive the isoepsilon curve for $\epsilon = -0.66$ (dotted line) and -0.76 (dashed line), Fig. 3(c).

For $\rho = 30$, the change in φ is small with respect to θ , Fig. 2 (d, +). In this regime, large changes in ϵ and γ yield small curvature variations in $\varphi(\theta)$. Since these variations are on the order of experimental noise, we found that multiple pairs of ϵ and γ fit the data. We, therefore, set $\epsilon = -0.66$ and -0.76 for $L/D = 40$ and 60 , respectively, and performed a single parameter fit to obtain γ . Although the linear dependence from the rest of the data does not hold, γ continues to increase with ρ , and the trend for $\mathcal{F}_{\text{bulk}}/\mathcal{F}_{\text{wall}}$ is well maintained. (Constraining both ϵ and γ to follow the trends of the other data did not yield good fits. Also, constraining γ to follow the linear trend resulted in an unrealistic single parameter fit of $\epsilon > 0$.) While the transition from bipolar to uniform patterning is continuous in nematic droplets [10], a pseudophase transition due to

finite size effects can be observed in more confined geometries [13]. The abrupt change in γ may result from such finite size effects.

In conclusion, even though our system of driven granular rods is far from the continuum limit and in a nonequilibrium steady state, we find that an equilibrium continuum description can capture many key features of the observed rod patterning. Moreover, we used this model to estimate the elastic anisotropy and relative wall anchoring for granular materials, thereby deepening the link to ideal hard rods. However, significant fluctuations in the patterning exist, for example nonpolar defects, that cannot be captured by this simple mean field description. Since granular materials commonly exhibit nonequilibrium patterning, it remains an open question whether these other defects result purely from finite sample size or also from nonequilibrium kinetics.

This research was supported by ISF Grants No. 1011/07 and No. 1012/07 (D. H.), NSF Grant No. NSF-DMR0907146 (W. L.), intramural funds from the Eunice Kennedy Shriver NICHD, and used the Biowulf computer cluster, NIH.

-
- [1] C. Josserand, A. V. Tkachenko, D. M. Mueth, and H. M. Jaeger, *Phys. Rev. Lett.* **85**, 3632 (2000); A. Kudrolli, G. Lumay, D. Volfson, and L. S. Tsimring, *Phys. Rev. Lett.* **100**, 058001 (2008).
 - [2] P. M. Reis, R. A. Ingale, and M. D. Shattuck, *Phys. Rev. Lett.* **96**, 258001 (2006); J. Stambaugh, K. Van Workum, J. F. Douglas, and W. Losert, *Phys. Rev. E* **72**, 031301 (2005).
 - [3] J. Galanis, D. Harries, D. L. Sackett, W. Losert, and R. Nossal, *Phys. Rev. Lett.* **96**, 028002 (2006).
 - [4] J. Galanis, R. Nossal, and D. Harries, *Soft Matter* **6**, 1026 (2010).
 - [5] H. Shin, M. J. Bowick, and X. Xing, *Phys. Rev. Lett.* **101**, 037802 (2008).
 - [6] J. Brugués, J. Ignés-Mullol, J. Casademunt, and F. Sagués, *Phys. Rev. Lett.* **100**, 037801 (2008).
 - [7] P. G. de Gennes and J. Prost, *The Physics of Liquid Crystals* (Oxford Science, New York, 1993), 2nd ed.
 - [8] A. V. Kaznacheev, M. M. Bogdanov, and S. A. Taraskin, *JETP* **95**, 57 (2002).
 - [9] P. Prinsen and P. van der Schoot, *Phys. Rev. E* **68**, 021701 (2003).
 - [10] P. Prinsen and P. van der Schoot, *Eur. Phys. J. E* **13**, 35 (2004).
 - [11] F. C. Frank, *Discuss. Faraday Soc.* **25**, 19 (1958).
 - [12] S. D. Hudson and E. L. Thomas, *Phys. Rev. Lett.* **62**, 1993 (1989).
 - [13] D. de las Heras, E. Velasco, and L. Mederos, *Phys. Rev. E* **79**, 061703 (2009).
 - [14] J. P. Straley, *Phys. Rev. A* **8**, 2181 (1973); S. D. Lee and R. B. Meyer, *J. Chem. Phys.* **84**, 3443 (1986).
 - [15] B. Tjipto-Margo, G. T. Evans, M. P. Allen, and D. Frenkel, *J. Phys. Chem.* **96**, 3942 (1992).
 - [16] R. B. Meyer, F. Lonberg, V. Taratuga, S. Fraden, S. D. Lee, and A. J. Hurd, *Faraday Discuss. Chem. Soc.* **79**, 125 (1985).